PLOS ONE

RESEARCH ARTICLE

Characterization of intrathecal cerebrospinal fluid geometry and dynamics in cynomolgus monkeys (*macaca fascicularis*) by magnetic resonance imaging

Mohammadreza Khani[1☯], Braden J. Lawrence[1,2☯], Lucas R. Sass[1], Christina P. Gibbs[1], Joshua J. Pluid[1], John N. Oshinski[3], Gregory R. Stewart[4,5], Jillynne R. Zeller[6], Bryn A. Martin[1]*

1 Department of Biological Engineering, University of Idaho, Moscow, ID, United States of America, **2** School of Medicine, University of Washington, Seattle, WA, United States of America, **3** Department of Radiology, Emory University, Atlanta, GA, United States of America, **4** Axovant, New York, NY, United States of America, **5** Voyager Therapeutics, Cambridge, MA, United States of America, **6** Northern Biomedical Research, Spring Lake, MI, United States of America

☯ These authors contributed equally to this work.
* brynm@uidaho.edu

Citation: Khani M, Lawrence BJ, Sass LR, Gibbs CP, Pluid JJ, Oshinski JN, et al. (2019) Characterization of intrathecal cerebrospinal fluid geometry and dynamics in cynomolgus monkeys (*macaca fascicularis*) by magnetic resonance imaging. PLoS ONE 14(2): e0212239. https://doi.org/10.1371/journal.pone.0212239

Editor: Quan Jiang, Henry Ford Health System, UNITED STATES

Received: December 17, 2018

Accepted: January 29, 2019

Published: February 27, 2019

Data Availability Statement: All relevant data are within the manuscript and its Supporting Information files.

Funding: This work was supported by Voyager Therapeutics, National Institutes of Health, National Institute of General Medical Sciences grant P20GM103408 and 4U54GM104944-04 and the University of Idaho, Vandal Ideas Project. Publication of this article was funded by the University of Idaho Open Access Publishing Fund.

Abstract

Recent advancements have been made toward understanding the diagnostic and therapeutic potential of cerebrospinal fluid (CSF) and related hydrodynamics. Increased understanding of CSF dynamics may lead to improved detection of central nervous system (CNS) diseases and optimized delivery of CSF based CNS therapeutics, with many proposed therapeutics hoping to successfully treat or cure debilitating neurological conditions. Before significant strides can be made toward the research and development of interventions designed for human use, additional research must be carried out with representative subjects such as non-human primates (NHP). This study presents a geometric and hydrodynamic characterization of CSF in eight cynomolgus monkeys (*Macaca fascicularis*) at baseline and two-week follow-up.

Results showed that CSF flow along the entire spine was laminar with a Reynolds number ranging up to 80 and average Womersley number ranging from 4.1–7.7. Maximum CSF flow rate occurred ~25 mm caudal to the foramen magnum. Peak CSF flow rate ranged from 0.3–0.6 ml/s at the C3-C4 level. Geometric analysis indicated that average intrathecal CSF volume below the foramen magnum was 7.4 ml. The average surface area of the spinal cord and dura was 44.7 and 66.7 cm^2 respectively. Subarachnoid space cross-sectional area and hydraulic diameter ranged from 7–75 mm^2 and 2–3.7 mm, respectively. Stroke volume had the greatest value of 0.14 ml at an axial location corresponding to C3-C4.

The funders had no role in study data collection and analysis, decision to publish, or preparation of the manuscript. Voyager Therapeutics had a role in the study design. Author GRS is employed by Axovant and was employed by Voyager Therapeutics during the course of this study. Axovant provided support in the form of salary for author GRS, but did not have any additional role in the study design, data collection and analysis, decision to publish, or preparation of the manuscript. Voyager Therapeutics provided support in the form of salary for author GRS. Author JRZ is employed by Northern Biomedical Research. Northern Biomedical Research provided support in the form of salary for author JRZ, but did not have any additional role in the study design, data collection and analysis, decision to publish, or preparation of the manuscript. The specific roles of these authors are articulated in the 'author contributions' section

Competing interests: I have read the journal's policy and the authors of this manuscript have the following competing interests: This study was funded in part by Voyager Therapeutics. Author GRS is employed by Axovant and was employed by Voyager Therapeutics during the course of this study. JRZ is a fulltime employee of Northern Biomedical. BAM has received grant support from Voyager Therapeutics, Alcyone Lifesciences, Biogen, and Minnetronix Medical; BAM is a member of the Neurapheresis Research Consortium. BAM is scientific advisory board member for Alcyone Lifesciences and the Chiari and Syringomyelia Foundation and served as a consultant to Voyager Therapeutics, SwanBio Therapeutics, Medtrad Biosystems, Neurosyntek, and Cerebral Therapeutics. There are no patents, products in development or marketed products to declare. This does not alter our adherence to all the PLOS ONE policies on sharing data and materials.

Introduction

Cerebrospinal fluid (CSF) is a clear, colorless fluid with water-like mechanical properties that bathes the entire brain and spinal cord. CSF plays a role in the protection of neural structures, metabolic homeostasis of the central nervous system (CNS), autoregulation of cerebral blood flow, and immunological support for neural tissue. CSF moves freely in an oscillatory manner with approximately zero net flow, and in synchrony with cardiac-related intracranial pulsations and respiration [1–5]. Recent advances have been made toward understanding the diagnostic and therapeutic potential of CSF and related hydrodynamics. Increased understanding of CSF dynamics may lead to improved detection of CNS diseases, development of CSF system-based intrathecal drug delivery, and improved treatment of debilitating neurological conditions.

The importance of CSF dynamics has been investigated in several CNS conditions including syringomyelia [6] Alzheimer's disease [7], Chiari malformation [8], and hydrocephalus [9]. Researchers have also applied computational fluid dynamics modeling approaches to understand how CSF dynamics related parameters could relate to CNS disease states and intrathecal drug delivery [10–14]. Before significant strides can be made toward the research and development of interventions designed for human consumption, additional research must be carried out with representative subjects such as non-human primates (NHP). However, relatively little information is known regarding CSF geometry and hydrodynamics in NHPs.

Studies have examined the possible role of CSF as a conduit for distribution of radiolabeled tracers [15] and therapeutic molecules to neuronal and glial cells of CNS tissues [16,17]. Intrathecal delivery of these molecules directly to the CNS tissue [2] is, in part, dependent on pulsation-dependent mixing of the spinal CSF dynamics. A solute injected into the CSF mixes [16], spreads throughout the CSF system, and is then taken up into the brain parenchyma via the perivascular (Virchow-Robbin) spaces [18,19]. Molecule injection to the CSF bypasses the blood-brain-barrier and allows delivery of many molecules that may not be possible through the systemic system [20,21]. The direct contact of CSF with neural tissue can enable delivery of small molecules to biologics including protein, cell-based, viral-mediated gene transfer, and gene therapies involving trophic factors to stimulate dying neurons [22,23]. These therapies have shown promise in animal studies [24,25] and safety in human clinical trials [26]. In addition, delivery in the CSF is a minimally invasive surgical intervention with a lower risk to the patient than other surgical interventions such as convection enhanced drug delivery and deep brain stimulation [25,27,28].

While intrathecal delivery of drugs or biologics to the CNS offers a promising treatment option, the dearth of knowledge has slowed therapeutic development and potentially confounded the analysis of therapeutic effectiveness. A common animal model used to test intrathecal therapeutics is the NHP, with one of the most common species being the cynomolgus monkey (*Macaca fascicularis*). Cynomolgus monkeys are a useful model for such studies since they are relatively compact compared to other NHP species, and share physiologic and cognitive similarities to humans. Despite being a frequently studied species, CSF hydrodynamic properties have not been studied or reported. At present, we do not know how NHP CSF hydrodynamics compare to humans or if they are consistent across animals and/or over time. The aim of the present study was to a) develop an MRI-based method to quantify intrathecal CSF dynamics in cynomolgus NHPs, b) use this method to quantify intrathecal CSF dynamics and geometry in a series of NHPs (N = 8), and c) measure the reliability of MRI-derived measures over a 2-week time interval.

Materials and methods

Ethics statement

This study was submitted to and approved by the local governing Institutional Animal Care and Use Committee at Northern Biomedical Research (IACUC approval #084-014A, Spring Lake, MI). This study did not unnecessarily duplicate previous experiments and alternatives to the use of live animals were considered. Procedures used in this study were designed with the consideration of the well-being of the animals.

Animals

MRI measurements were obtained for eight (NHP 01–08) healthy five-year-old adult cynomolgus monkeys (Macaca fascicularis, origin Mauritius) from Charles River Research Models, Houston TX with a weight of 4.4 ± 1.2 kg (mean ± standard deviation). NHP 01 was male. All other NHPs were female (02–08). These animals were purpose-bred and experimentally naïve. Each NHP was scanned with an identical protocol at baseline and at follow-up after a 2-week time interval.

MRI scan protocols

All MRI measurements were acquired at Northern Biomedical Research (Muskegon, Michigan, U.S.A.) on a Philips 3T scanner (Achieva, software V2.6.3.7, Best, The Netherlands). Prior to MRI scanning each NHP was prepared using standard procedures and precautions. NHPs were positioned in the scanner in the supine position without assistance from artificial respiration. During each scan, heart rate and respiration was monitored continuously with ~ 1 liter/minute of oxygen and 1–3% isoflurane anesthetic administered via endotracheal tube for sedation.

Anatomic MRI scan protocol for CSF space geometry quantification

Total scan time to quantify CSF space geometry and flow (including NHP MRI preparation) for each NHP was ~1 hour after the protocols were in place. A stack of high-resolution axial T2-weighted MR images of the complete spinal subarachnoid space (SAS) geometry was acquired for each NHP using a VISTA (31 minutes) protocol (**Table 1**). The anatomical region scanned was ~30 cm in length, which included the intrathecal SAS below the lower brain stem extending caudally to the filum terminale. This comprised a total of ~720 images with 0.5 mm slice spacing, 1.0 mm slice thickness, and 0.375 mm isotropic in-plane resolution.

Phase-contrast MRI scan protocol for CSF flow quantification

Thru-plane (head-foot, z-direction) CSF flow was measured by phase-contrast MRI (PC-MRI) images collected at six axial locations along the spine for each NHP. Axial locations were located at the foramen magnum (FM), C2-C3, C5-C6, T4-T5, T10-T11, and L3-L4 and required ~3 minutes scan time per location. Flow images were acquired with a retrospective ECG triggered sequence with 24 heart phases, 0.45 mm isotropic in plane resolution, and 5 mm slice thickness (**Table 1**). Slice location for each scan was oriented approximately perpendicular to the CSF flow direction with slice planes intersecting vertebral discs. More details on the PC-MRI protocol are given in Martin et al. [29].

3D image segmentation

The high-resolution T2-weighted anatomic MRI images were semi-automatically segmented using the free open-source ITK-snap software (Version 3.0.0, University of Pennsylvania, U.S.

Table 1. Anatomic (T2-VISTA) and CSF flow (phase-contrast MRI) scan protocol parameters used for imaging cynomolgus monkeys.

Parameter	Anatomic (T2-VISTA)	CSF Flow (PC-MRI)
File size	941 MB	7 MB
Acquisition contrast	T2	Flow encoded
Acquisition type	3D	2D
Slice Thickness	1 mm	5 mm
Slice spacing	0.5 mm	N/A
Pixel bandwidth	481	192
Pulse Sequence	TSE	TFE
Transmit coil	Body	Body
Duration	31 minutes	200–240 seconds
Number of slices	660	N/A
Image matrix	864 x 864	224 x 224
In-plane resolution	0.375 mm	0.446 mm
Repetition time	2000 (ms)	11.226–12.704 (ms)
Echo Time	120 (ms)	6.749–8.226 (ms)
Cardiac phases	N/A	24
R-R interval	N/A	454–653 ms
Encoding direction	N/A	Thru-plane
Plane orientation	Sagittal	Axial
Trigger	N/A	Retrospective ECG
Velocity encoding	N/A	5 at FM and L4; 10 elsewhere

https://doi.org/10.1371/journal.pone.0212239.t001

A.) [30], which provided semi-automatic segmentation using active contour methods, as well as manual delineation and image navigation (Fig 1). The manual segmentation tool was used most frequently with view of the three orthogonal planes. Detailed information on the segmentation procedure is provided by Martin et al. [31]. Once the segmentation was complete, the 3D model was exported in a .STL (Stereo Lithography) format for subsequent analysis as outlined below.

CSF flow waveform and profile analysis

CSF flow was quantified at six axial locations along the spine (Fig 2) using GTFLOW software (64-bit, Version 2.2.10, Gyrotools, Zurich, Switzerland) by the following procedure previously described in [31]. PC-MRI and corresponding magnitude images were loaded into GTFLOW. A region of interest (ROI) was created within the area of CSF flow between the dura and spinal cord (Fig 2A). Individual pixel velocities within each ROI were exported to a .CSV (Comma-Separated Values) file for further analysis using MATLAB software (Ver. R2016a Mathworks Corp., Natick, MA). CSF flow waveform within the ROI, $Q(t)$, was computed with $Q(t) = \Sigma A_{pixel} V_{pixel}(t)$, where A_{pixel} is the area of one MRI pixel, $V_{pixel}(t)$ is the velocity for the corresponding pixel at any time, and $Q(t)$ is the summation of the flow for each pixel within the ROI. The CSF flow waveform was offset to ensure zero net flow over the flow cycle since CSF flow in the spine has approximately zero net flow (oscillatory).

The following method was applied to generate a smooth spatial-temporal CSF flow distribution, $Q(z,t)$, along the spine. The axial phase-contrast slice locations were not identical for each NHP due to differences of the exact vertebral levels across cases. Thus, the z-location of each slice was manually measured based on the distance of that slice caudal to the FM (Table 2). The six distinct flow rates were smoothed in a spatial-temporal fashion using

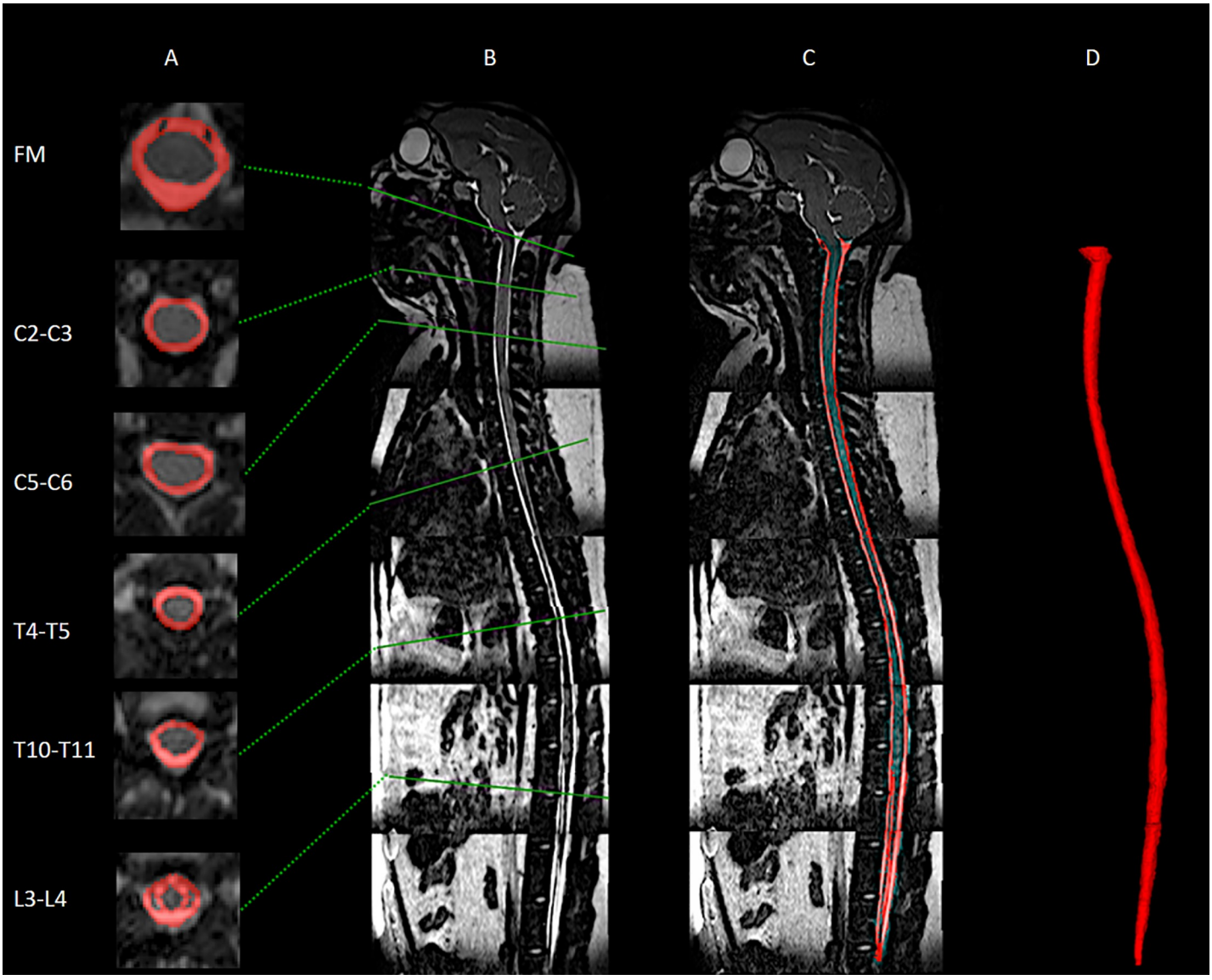

Fig 1. Manual segmentation of the spinal subarachnoid space using a T2-weighted MR image for a cynomolgus monkey analyzed in this study. (A) Visualization of SAS area manually selected around the spinal cord at multiple axial levels. (B) Mid-sagittal high-resolution T2-weighted MRI. (C) Sagittal visualization of segmented SAS around the spinal cord. (D) 3D visualization of entire SAS geometry. The same methods were applied to all MR images obtained for all NHPs.

https://doi.org/10.1371/journal.pone.0212239.g001

MATLAB and a 2D "fit" function with the fit-type designated as "smoothing-spline". Since heart rate variability was present between the PC-MRI scans, the CSF flow waveform timing was normalized to the average heart rate for all NHPs. An average spatial-temporal CSF waveform was determined. CSF pulse wave velocity, *PWV*, was computed based on the slope of the arrival time of peak CSF flow along the spine [32].

Geometric and hydrodynamic parameter quantification

Several geometric and hydrodynamic parameters were calculated based on the 3D segmentation and flow analysis using our previously published methods [11]. Using the exported 3D . STL file (above), each of these parameters was calculated by a user-defined function (UDF)

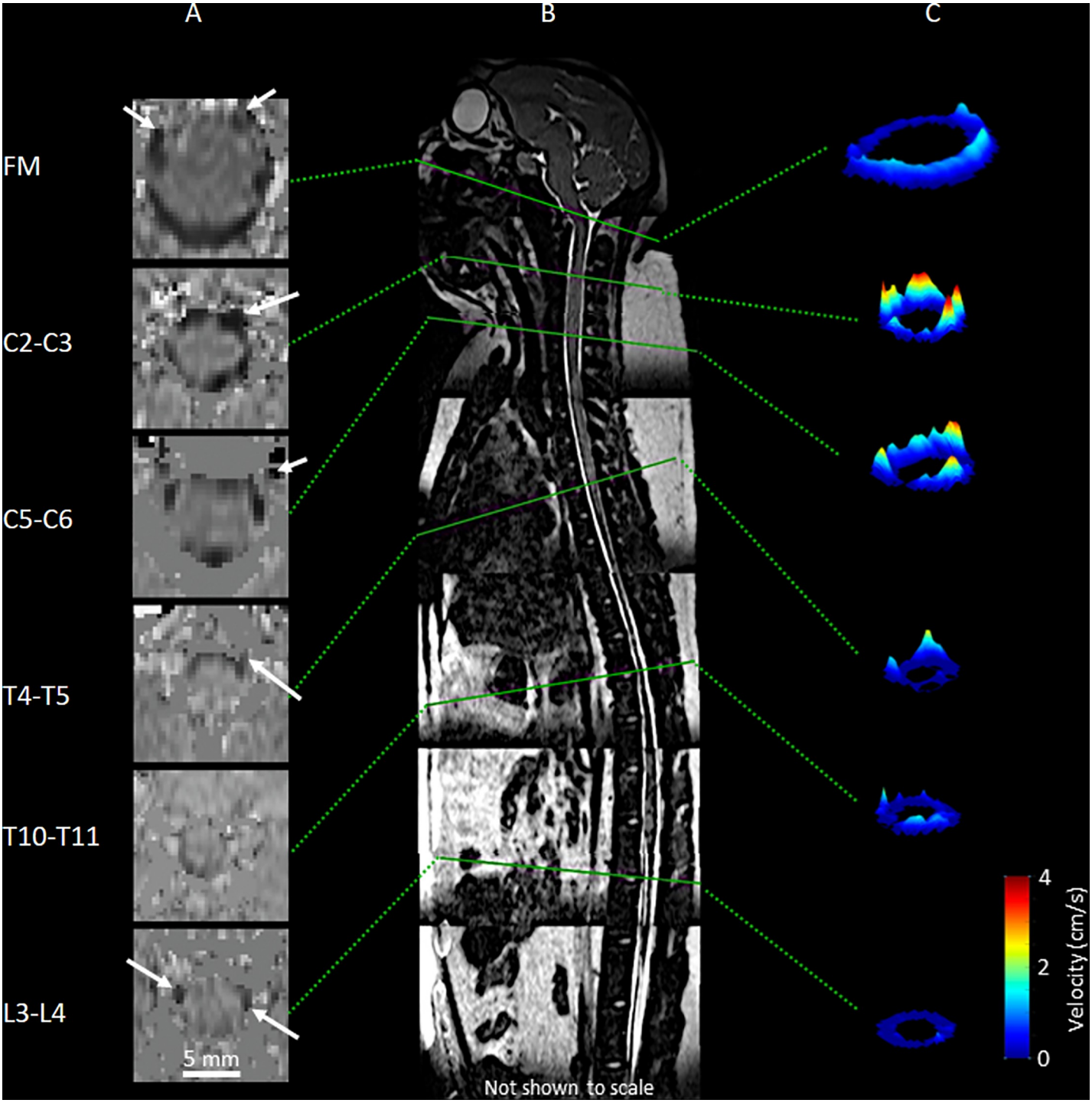

Fig 2. Axial PC-MRI and CSF velocity profiles at corresponding vertebral levels for a cynomolgus monkey in this study. (A) PC-MRI axial cross-sections for a given case at each respective vertebral level. (B) T2-weighted MR image of a cynomolgus monkey in the study with corresponding PC-MRI axial locations and slice orientation (solid green lines) at FM, C2-C3, C5-C6, T4-T5, T11-T12, and L3-L4. (C) 3D visualization of peak systolic CSF velocity profiles based on in vivo PC-MRI measurements at each vertebral level.

https://doi.org/10.1371/journal.pone.0212239.g002

compiled in ANSYS FLUENT (ANSYS Academic Research, Release 19.1, Canonsburg, PA, USA) based on a computational mesh generated from ANSYS ICEM (ANSYS Academic

Table 2. Reference chart for vertebral disk location with respect to axial distance from the foramen magnum in cynomolgus monkeys.

Vertebral level	Mean ± std (mm)
'FM'	0.0 ± 0.0
'C1'	5.7 ±2 .4
'C2'	10.3 ± 2.6
'C3'	22.3 ± 3.9
'C4'	29.0 ± 3.6
'C5'	35.2 ± 3.8
'C6'	42.2 ± 3.4
'C7'	48.7 ± 3.8
'T1'	56.1 ± 4.2
'T2'	63.4 ± 4.4
'T3'	72.0 ± 4.2
'T4'	79.8 ± 4.2
'T5'	88.5 ± 4.5
'T6'	97.9 ± 4.9
'T7'	107.4 ± 4.5
'T8'	117.6 ± 4.8
'T9'	128.8 ± 4.5
'T10'	141.4 ± 5.4
'T11'	156.3 ± 5.0
'T12'	172.0 ± 5.1
'L1'	189.6 ± 5.4
'L2'	207.5 ± 5.8
'L3'	227.1 ± 6.8
'L4'	247.0 ± 7.0
'L5'	268.9 ± 6.2
'Sacrum'	289.4 ± 6.7
'coccyx'	301.0 ± 6.8

FM = Foramen magnum, C = Cervical, T = Thoracic, L = Lumbar

https://doi.org/10.1371/journal.pone.0212239.t002

Research, Release 19.1, Canonsburg, PA, USA). Details on the methods used to generate each parameter are as follows.

The following parameters were computed based on overall spine geometry: Total SAS surface area, SA_{sas}, was calculated as the sum of surface area of spinal cord, SA_c, and dura, SA_d. Spinal cord nerve roots were not included in the surface area calculation of the cord since these small features were not possible to accurately visualize by MR imaging. Total volume of the SAS, V_{sas}, was computed by subtracting the volume of the spinal cord, V_c from the volume of the dura, V_d. An overall average, maximum, and minimum value was then computed across all NHPs. Total SAS length, L_{sas}, from the FM to the SAS termination was quantified.

The following parameters were determined for each 1 mm interval along the spine (z-location): Axial distribution of the SAS cross-sectional area, $A_{sas}(z)$, was based on cross-sectional area of the spinal cord at that location, $A_c(z)$, and dura, $A_d(z)$. Similarly, hydraulic diameter, $D_h(z) = 4A_{sas}(z)/P_{sas}(z)$, was determined based on the wetted perimeter, $P_{sas}(z)$, with the perimeter computed as the sum of the spinal cord, $P_c(z)$, and dura, $P_d(z)$, perimeters at each z-location. Axial distribution of CSF stroke volume was computed as $SV(z) = \int|Q(z,t)|dt$, where $|Q(z,t)|$ is the absolute value [33]. Peak systolic (toward feet) and diastolic (toward head) CSF

flow rate was quantified as $Q_{sys}(z)$ and $Q_{dia}(z)$, and the CSF flow rate amplitude was given by $Q_a(z) = Q_{dia}(z) - Q_{sys}(z)$. Spatial mean thru-plane velocity at peak systole was computed as $\bar{U}_{sys}(z) = Q_{sys}(z)/A_{sas}(z)$ and at diastole as $\bar{U}_{dia}(z) = Q_{dia}(z)/A_{sas}(z)$. Reynolds number was computed as $Re(z) = (\bar{U}_{sys}(z) \cdot D_h(z))/\nu$, were ν is the kinematic viscosity of CSF at body temperature, 0.693 mPa·s [29]. Womersley number was computed as $\alpha(z) = \frac{D_h(z)}{2}\sqrt{\omega/\nu}$, where ω is the angular velocity ($\omega = 2\pi/T$) of the volume flow waveform with T equal to the heart rate.

To allow parameter comparison across NHPs, each parameter's axial distribution for each NHP was normalized to the average L_{sas} measured for all NHPs. After normalization, the mean axial distribution for each parameter was computed across all NHPs. The mean axial distribution was then used to obtain an average, maximum, and minimum parameter value along the spine based on all NHPs.

Parameter reliability

Reliability was assessed by obtaining MRI measurements for each NHP at baseline and 2-week follow-up while ensuring identical methods during both collection intervals. To quantify measurement reliability, we performed a regression of baseline versus follow-up parameters computed at each axial location along the spine. All computations and plots were generated using MATLAB software (Ver. R2016a Mathworks Corp., Natick, MA).

Results

Results were obtained for a total of eight NHPs at baseline and a 2-week follow-up time point (Table 3). Overall, the MRI protocol allowed quantification of all proposed geometric and hydrodynamic parameters. These parameters had a relatively similar axial distribution across all NHPs analyzed and were similar at follow-up for each NHP. CSF flow was laminar in all NHPs with the greatest degree of CSF motion observed in the cervical spine. Average results showed that maximum Re and α was 80 and 7.7, respectively. A_{sas} and D_h ranged from 7–75 mm^2 and 2–3.7 mm, respectively. Maximum $\bar{U}_{sys}$ and $\bar{U}_{dia}$ was -2.7 to 1.6 cm/s and located in the cervical spine. SV ranged from 0.14 ml in the cervical spine to roughly 0 ml in the lower lumbar spine for all NHPs.

Geometric parameters

Average V_{sas} for all NHPs was 7.41 ml. Average SA_c and SA_d was 44.74 ± 3.52 and 66.66 ± 3.11 cm^2 respectively. A_{sas} and D_h decreased moving caudally down the spinal cord from the FM (Fig 3). The minimum value for A_{sas} and D_h was 7 mm^2 and 2 mm, respectively (Table 3). These values occurred at ~70 mm caudal to the FM, a location approximately corresponding to T2-T3 (Table 2). Maximum difference in A_{sas} and D_h between NHPs at any axial location (omitting the FM) was ~30 mm^2 and 4 mm, respectively.

CSF flow waveforms

$Q(t)$ of each NHP quantified along the spine had a similar waveform shape, magnitude and axial distribution (Fig 4). $Q(t)$ shape showed a well-defined systolic peak at 100 to 300 ms (negative flow) followed by a diastolic peak that varied based on the heart rate (similar to cardiac blood flow). Q_{sys} ranged from 0.35–0.87 (ml/s) at the C3-C4 level for all NHPs. $Q(t)$ at the FM was markedly smaller than at C3-C4. Caudal to C3-C4, $Q(t)$ had a decreasing trend in magnitude moving down the spine. The CSF flow was found to be nearly zero in all PC-MRI scans before eddy current offset correction. Maximum average CSF flow offset was 13% relative to the arithmetic mean of the absolute CSF flow.

Table 3. Summary of geometric and hydrodynamic results. Mean values correspond to the average along the entire spine for all 16 NHPs (except for total surface area, volume, and *PWV*). Local maximum and minimum values are computed based the average for all 16 NHPs.

Parameter	Symbol	Unit	Average	Maximum	Minimum
Parameters computed at 1 mm intervals along the spine					
Perimeter of spinal cord	P_c	*mm*	14.77	62.02	0.73
Perimeter of dura	P_d	*mm*	22.06	38.63	9.54
Perimeter of subarachnoid space	P_{sas}	*mm*	36.82	99.56	10.50
Area of spinal cord	A_c	mm^2	15.05	81.50	0.50
Area of dura	A_d	mm^2	39.59	137.45	7.61
Area subarachnoid space	A_{sas}	mm^2	24.54	75.10	6.98
Hydraulic diameter	D_h	*mm*	2.68	3.73	2.02
Reynolds number	*Re*	*NA*	29.30	79.27	0.66
Womersley number	α	*NA*	5.50	7.67	4.15
Mean velocity at peak systole	$\bar{U}_{sys}$	*cm/s*	-0.83	-0.02	-2.69
Mean velocity at peak diastole	$\bar{U}_{dia}$	*cm/s*	0.58	1.59	0.02
Flow rate at peak systole	Q_{sys}	*ml/s*	-0.20	0.00	-0.60
Flow rate at peak diastole	Q_{dia}	*ml/s*	0.14	0.35	0.00
Flow rate amplitude	Q_a	*ml/s*	0.33	0.94	0.00
Stroke volume	*SV*	*ml*	0.05	0.14	0.00
Parameters computed based on the entire spine					
Surface area of spinal cord	SA_c	cm^2	44.74	49.63	37.76
Surface area of dura	SA_d	cm^2	66.66	70.49	60.53
Surface area of subarachnoid space	SA_{sas}	cm^2	111.39	120.12	98.31
Volume of spinal cord	V_c	*ml*	4.57	5.40	3.98
Volume of Dura	V_d	*ml*	11.99	13.45	10.25
Volume of subarachnoid space	V_{sas}	*ml*	7.41	8.47	6.24
Length of subarachnoid space	L_{sas}	*mm*	301	306.98	295.80
Pulse wave velocity	*PWV*	*m/s*	1.13	3.45	0.73

https://doi.org/10.1371/journal.pone.0212239.t003

Average spatial-temporal $Q(t)$ distribution across all NHPs showed a relatively smooth decrease in amplitude along the spine and had relatively small, if any, wave reflections from the SAS termination (Fig 5B). Spatial temporal $Q(t)$ distribution showed that maximum CSF flow rate occurred ~25 mm caudal to the FM (Fig 5B). $Q(t)$ shape and magnitude were similar from ~125 mm to the SAS termination.

Hydrodynamic parameters

SV ranged from ~0 to 0.14 ml along the spine and had the greatest value at the axial location corresponding to C3-C4 (Fig 6). Difference in *SV* between NHPs was a maximum of ~ 0.1 ml at the upper cervical spine (C3-C4).

A noticeable phase shift was observed in the $Q(t)$ along the spine (Fig 4). This phase shift is thought to be representative of intrathecal space stiffness or compliance and can be quantified in terms of *PWV*. Based on the time of Q_{sys} at the FM versus the lumbar spine, *PWV* was estimated to be vary from 0.73 to 3.45 m/s among NHPs with an average value of 1.13 m/s (Table 3).

Re had a decreasing trend moving caudally along the spine (Fig 6A). *Re* varied from 80 in the cervical spine to 0 at the most caudal region, with the maximum value located at C3-C4 level. Local difference in *Re* among the NHPs was a maximum of ~75 and located within the

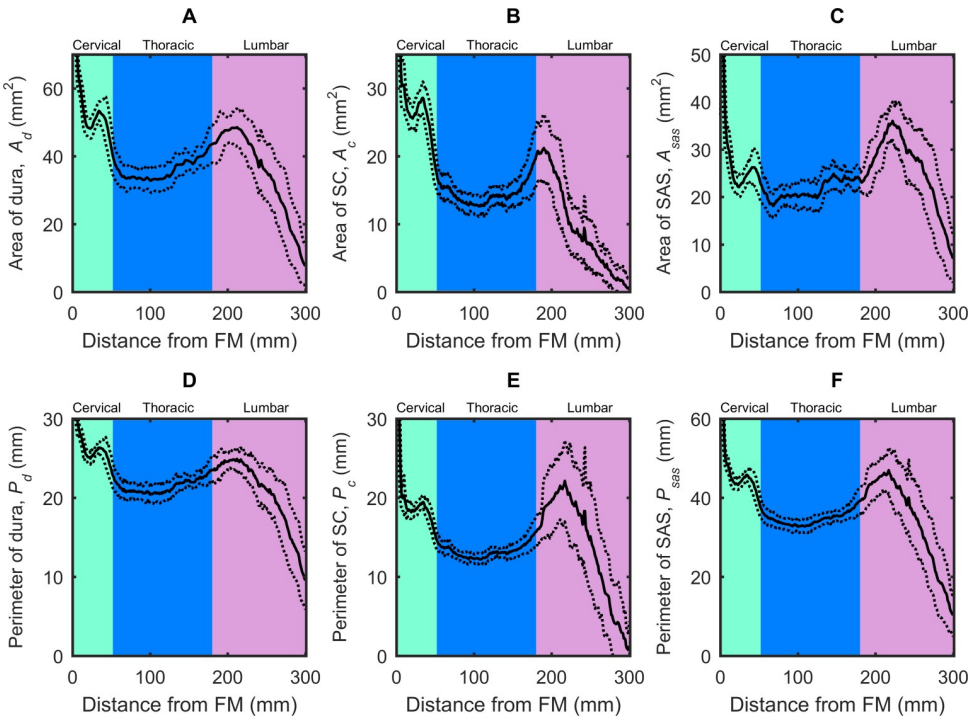

Fig 3. Geometric parameters distribution computed along the spine for cynomolgus monkeys. (A) Area of dura, (B) Area of spinal cord, (C) Area of subarachnoid space, (D) Perimeter of dura, (E) Perimeter of spinal cord, (F) Perimeter of subarachnoid space. Mean value for all 16 NHPs corresponds to the solid line. Dotted lines correspond to ± 1 standard deviation for all 16 NHPs analyzed.

https://doi.org/10.1371/journal.pone.0212239.g003

cervical spine. α ranged from 4 to 7.7, with a maximum value located near the FM (Fig 6D, right axis).

The peak value of the $\bar{U}_{dia}$ and $\bar{U}_{sys}$ ranged from +1.6 to -2.7 cm/s and occurred at the C3-C4 level (Fig 6E). $\bar{U}$ was smaller at the FM compared to C3-C4 for all NHPs. As expected, these alterations in $\bar{U}$ were inversely related to A_{sas}; axial locations with largest A_{sas} (FM, see Table 3 and Fig 3) demonstrated reduced velocities compared to areas with smaller A_{sas} and their respective increased velocities.

Parameter reliability

There was relatively good agreement between the baseline and follow-up MRI scans across all parameters confirming the reproducibility of the method. Differences between geometrics and hydrodynamic parameters obtained from the baseline to the follow-up MRI scan were quantified using regression analysis as shown in **Figs** 7 and 8. The results correspond to all eight NHPs and are plotted for the entire spine model between baseline and follow-up (from FM to the SAS termination).

Strong correlation was observed from the linear regression analysis for P_d ($R^2 = 0.84$, $slope = 0.98$), P_c ($R^2 = 0.80$, $slope = 0.93$), and P_{sas} ($R^2 = 0.85$, $slope = 0.97$). Correlation was stronger for the A_d ($R^2 = 0.88$, $slope = 0.95$) and A_c ($R^2 = 0.88$, $slope = 0.94$), but was slightly weaker in A_{sas} ($R^2 = 0.77$, $slope = 0.90$).

The second set of regression plots (Fig 8) showed that the value of discrepancy between baseline and follow-up results could be higher for hydrodynamic parameters. There was a relatively weak correlation for α and D_h ($R^2 = 0.41$, $slope = 0.72$). Relative to geometric results,

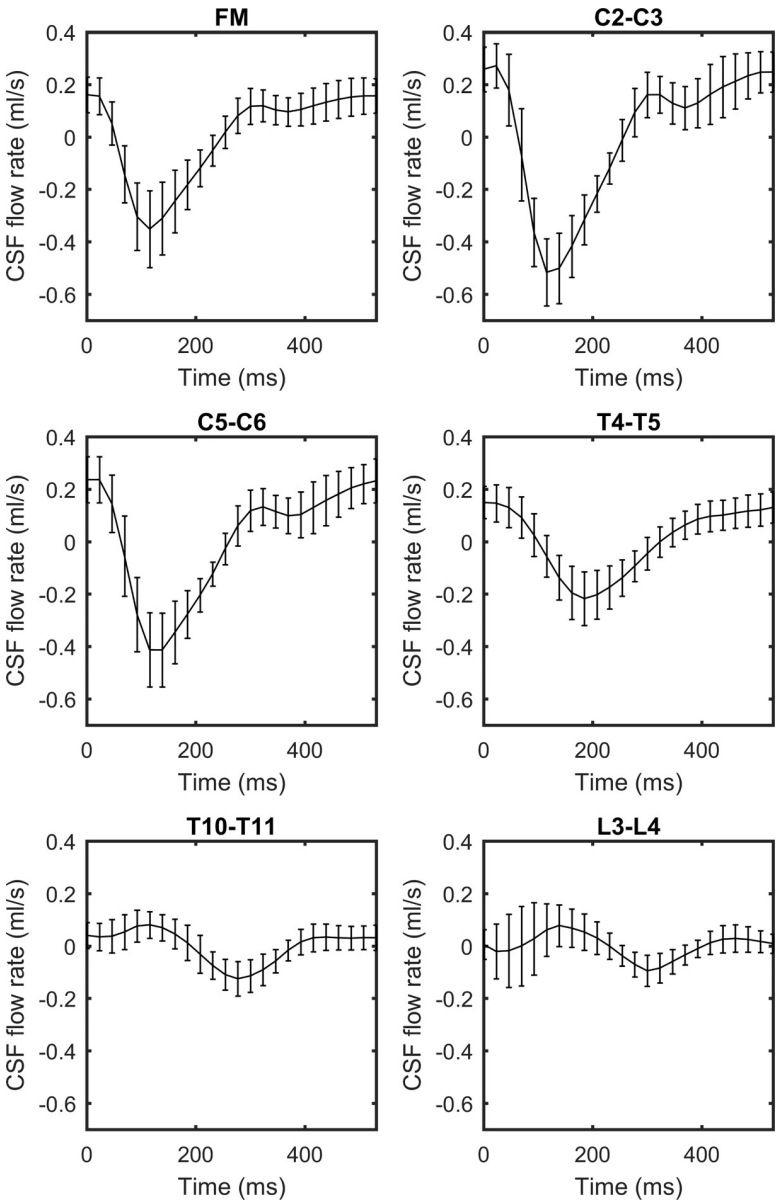

Fig 4. CSF flow waveforms for all 16 cases measured by PC-MRI at six axial locations along the spine. Error bars correspond to ± 1 standard deviation of flow rates obtained for all 16 NHPs. Note: negative, or peak systolic, CSF flow is in the caudal direction.

https://doi.org/10.1371/journal.pone.0212239.g004

there was additional discrepancy for flow parameters related to $\bar{U}$ ($R^2 = 0.72$, *slope* = 0.93), Q_a ($R^2 = 0.63$, *slope* = 0.88), and SV ($R^2 = 0.75$, *slope* = 0.90), though not to the degree as the α and D_h.

Discussion

This study presents a method and results for detailed characterization of intrathecal CSF geometry and hydrodynamics in cynomolgus monkeys (*Macaca fascicularis*). Results show that CSF geometry and dynamics can be reliably detected using non-invasive MRI measurements and that results are consistent for cynomolgus monkeys of a similar size and age.

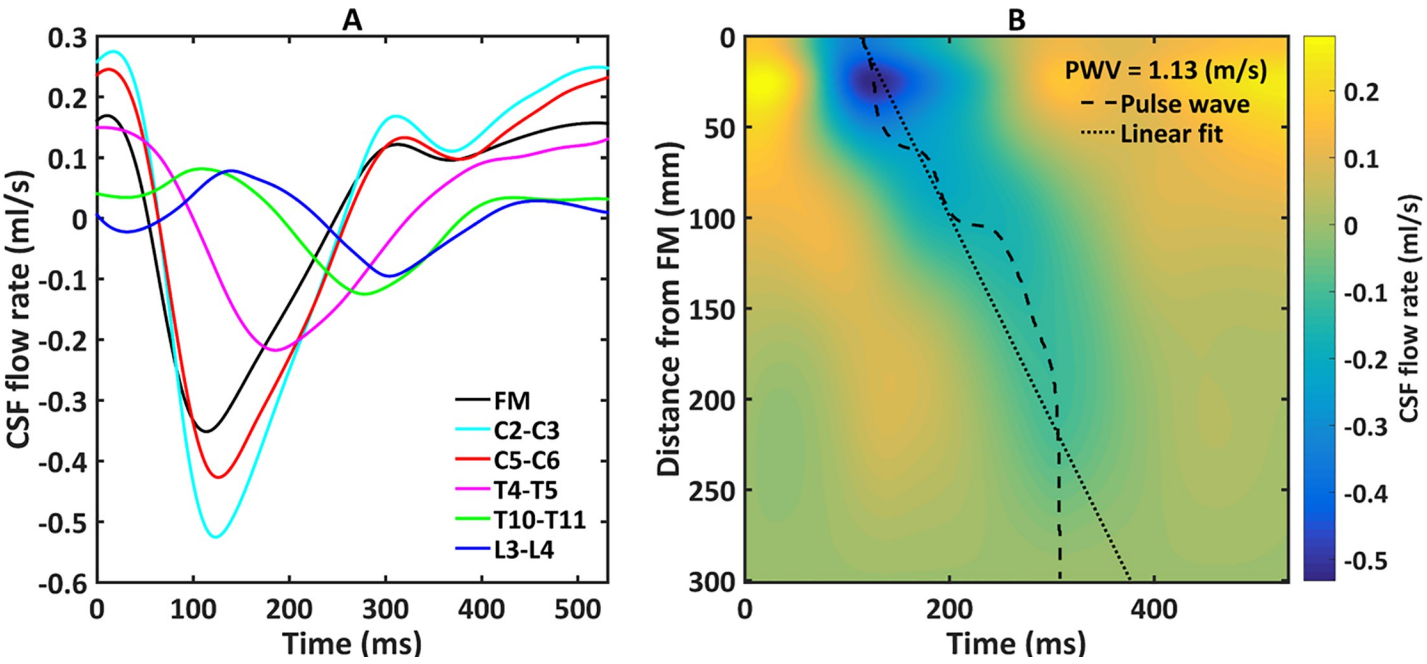

Fig 5. Mean CSF flow waveforms and Spatial-temporal distribution of CSF flow rate. (A) Mean CSF flow waveforms for all 16 cases measured by PC-MRI at six axial locations along the spine. Note: negative, or peak systolic, CSF flow is in the caudal direction. (B) Spatial-temporal distribution of the interpolated CSF flow rate along the spine. Dotted line indicates peak CSF flow rate at each axial level used to compute CSF pulse wave velocity (*PWV*).

https://doi.org/10.1371/journal.pone.0212239.g005

Nature of CSF dynamics in cynomolgus monkeys

Our results show that CSF moves in a smooth oscillatory manner along the entire spinal axis of cynomolgus NHPs. Chaotic velocity or pressure fluctuations are not expected and transverse CSF velocities (non-streamwise) are likely small compared to axial velocities. CSF dynamics were found to be most active in the cervical spine near the C3-C4 vertebral level with a maximum *Re* of 80 (Table 3 and Fig 6). *Re* was computed to represent the ratio of steady inertial forces to viscous forces and help indicate whether laminar flow ($Re<2300$) was present at each phase contrast slice location (Fig 6 and Table 3). A laminar CSF flow indicates that the flow is smooth with relatively little lateral mixing. This is different from a turbulent flow, where chaotic changes in pressure and velocity occur and can lead to a large increase in lateral mixing. Thus, CSF flow is expected to remain laminar throughout the CSF flow cycle as the *Re* remained sub-critical ($Re_{critical} = 2100$) for all NHPs analyzed. However, it is possible that disease states that result in strongly elevated CSF flow velocities (jets) could result in turbulence [34].

Inertial effects are expected to dominate the SAS CSF flow field for normal physiological flow rates, frequencies and CSF fluid properties. α varied in the same fashion as D_h with a minimum and maximum value of 4.1 and 7.7 (Table 3 and Fig 6). α, was computed to quantify the ratio of unsteady inertial forces to viscous forces that impact the CSF velocity profile shape [35]. For $\alpha<1$, the CSF velocity profiles will be parabolic in shape. $\alpha>10$ will result in relatively flat or plug-like velocity profiles [36]. This means that the CSF velocity profiles will have a plug-like shape throughout the spine. Albeit, flows in an annulus may be less inertial compared to pipe flows of the same α [35]. Our previous computational fluid dynamics NHP model indicated a relatively blunt CSF velocity profile in the cervical spine [11]. It is difficult to confirm if the in vivo velocity profiles measured in the current study were in fact blunt shaped (Fig 2C)

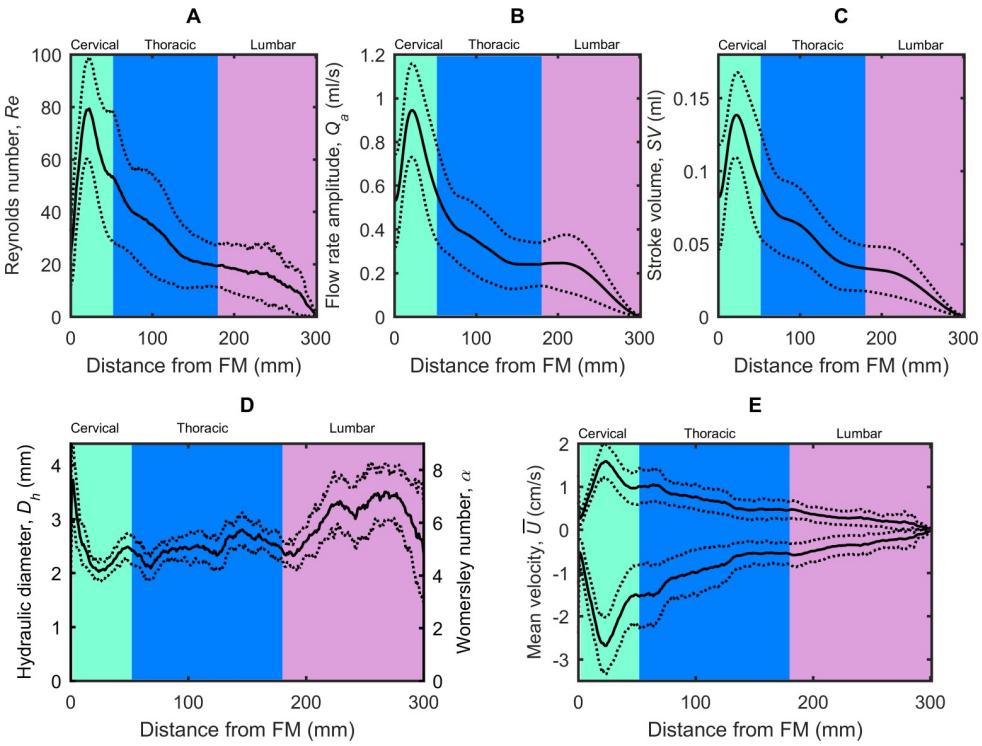

Fig 6. Hydrodynamic parameter distribution computed along the spine for cynomolgus monkeys. (A) Reynolds number, *Re*, (B) Flow rate amplitude, Q_a, (C) Stroke Volume, *SV*, (D) left axis, Hydraulic diameter, D_h, right axis, Womersley number, α, (E) mean peak systolic, $\bar{U}_{sys}$, and diastolic, $\bar{U}_{dia}$, CSF velocity. Mean value for all 16 NHPs corresponds to the solid line. Dotted lines correspond to ± 1 standard deviation for all 16 NHPs analyzed.

https://doi.org/10.1371/journal.pone.0212239.g006

as the MRI resolution was not fine enough to accurately capture the relatively thin boundary layer expected in a blunt flow profile.

CSF pulse wave velocity along the spine

With each heartbeat, a cardiac-induced CSF pulse wave was found to travel in the cranial-caudal direction (downwards) at a rate of *PWV*~ 1.13 m/s (Fig 5B). This wave appeared to be damped along the spinal axis and had relatively little reflection due to the SAS termination. This *PWV* is similar to the study previously reported by our group [11] for one cynomolgus monkey. CSF *PWV* studies have been conducted for humans. Williams obtained simultaneous invasive recordings of ventricular and lumbar CSF pressure in humans during various maneuvers such as coughing and valsalva [37]. From these recordings, a CSF *PWV* can be estimated to range from 8–4 m/s, after coughing. Kalata et al. used high-speed PC-MRI to quantify the CSF velocity wave speed in a small portion of the cervical spine (~20 cm) and found it to be 4.6 ± 1.7 m/s [32]. Another study by Sweetman et al. predicted spinal CSF *PWV* to be ~3 m/s [38]. Martin et al. used a numerical 1-D tube model of the spinal SAS to analyze the effect of dura mechanical properties on spinal CSF flow and pressures and they found CSF *PWV* varied from 2.5 to 13.5 m/s depending on dura elasticity [39]. They also investigated spinal CSF wave phenomena using *in vitro* models and found CSF wave reflections to be present [40]. Similar conclusions have been reported by other groups with different approaches and numerical simulations [41–44]. Results in this study did not show a large degree of CSF wave reflection within the spine (Fig 5B).

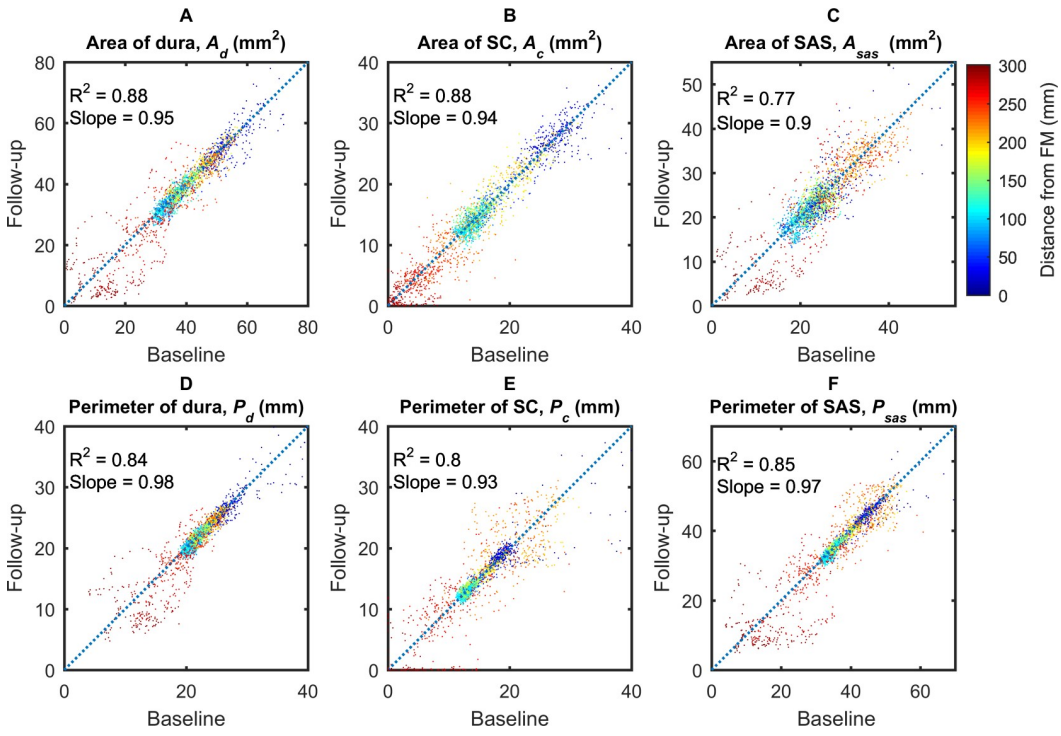

Fig 7. Scatter plots of geometric parameters. (A) Area of dura, (B) Area of spinal cord, (C) Area of subarachnoid space, (D) Perimeter of dura, (E) Perimeter of spinal cord, (F) Perimeter of subarachnoid space. Dot color represents distance from the FM (blue is near the FM and red is near the SAS termination).

https://doi.org/10.1371/journal.pone.0212239.g007

Arterial *PWV* has been found to have important implications in several vascular diseases [45,46]. Spinal CSF *PWV* could also have implications on perivascular transport in context of syringomyelia [47–49]. Further study is necessary to understand CSF *PWV* in the spine and its relevance CNS physiology in health and disease.

Geometric and hydrodynamic characterization

To the best of our knowledge, axial variation in spinal SAS geometry in terms of A_c, P_c, and D_h in a cynomolgus monkey has not been reported in the literature. This may be due, in part, to the relatively long time period (55 minutes total) required to obtain the high-resolution MRI images (375 μm isotopic) used to segment the CSF space in this study. Geometric parameters such as A_d, A_c, A_{sas}, P_d, P_c, and P_{sas} were shown to vary significantly along the spine. Hydrodynamic parameters such as D_h, Re, α, $\bar{U}$, Q_a and SV also varied significantly along the spinal canal due to the changes in geometry. CSF flow measurements in the cervical spine by MRI were used to estimate flow values of hydrodynamic parameters. The variation in A_{sas} is significant ~7 to 75 mm^2 (see **Fig 3B**), which indicates fluid acceleration may be significant in the spinal cavity near the skull and base of the spine. D_h ranged from ~1.5–4.5 mm in all NHPs analyzed. The axial distribution of SAS geometry in the cynomolgus monkey had a similar trend as that quantified in humans for A_c, P_c, and D_h [29], albeit approximately ~7.4, 2.3, and 2.4 times smaller, respectively, in magnitude compared to a human [35].

Average V_{sas} for all NHPs in this study was ~7.41 ml. To our knowledge, V_{sas} has not been measured in NHPs. However, total NHP CSF volume is typically considered to range from 12–15 mL in CSF dosing studies [50]. Our results indicate that the total NHP CSF volume in these studies is likely to be underestimated by approximately a factor of 2. Similarly, recent

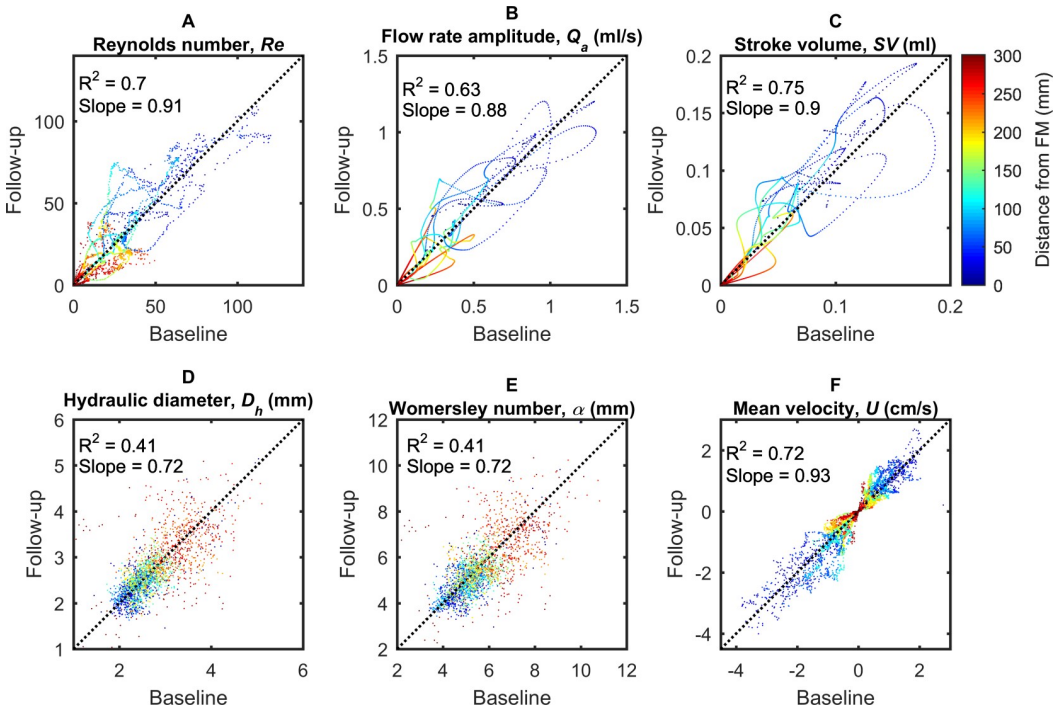

Fig 8. Scatter plots of hydrodynamic parameter distribution computed along the spine. (A) Reynolds number, *Re*, (B) flow rate amplitude, Q_a, (C) stroke volume, *SV*, (D) hydraulic diameter, D_h, (E) Womersley number, α, and, (F) mean peak systolic, $\bar{U}_{sys}$, and diastolic, $\bar{U}_{dia}$, CSF velocity. Dot color represents distance from the FM (blue is near the FM and red is near the SAS termination).

https://doi.org/10.1371/journal.pone.0212239.g008

studies in humans show that total CSF volume is not 150 mL as reported in the traditional literature [51]. Recent researchers using high-resolution non-invasive MRI-based methods have reported the total CSF volume to be approximately two times larger, ranging from 250–400 mL [52,53]. Detailed MRI investigation of the complete CSF space in terms of its geometry is lacking in the literature.

Measurement reliability

To help understand parameter reliability, we collected MRI images for 8 NHPs at two time points separated by a two-week time interval. Results showed a relatively strong degree of parameter reliability for all geometric-based parameters (A_d, A_c, A_{sas}, P_d, P_c, and P_{sas} in Fig 7) and to a lesser degree for hydrodynamics based parameters (D_h, *Re*, α, $\bar{U}$, Q_a and *SV* in Fig 8). The reason for lower degree of reliability for hydrodynamic parameters is likely because these parameters incorporate input from both flow and geometry, both of which will have associated error and/or natural physiologic variation in NHPs. It should also be noted that we do not expect all parameters to remain identical at the 2-week follow-up time point as CSF flow can be altered due to posture, sedation, and other factors that were not specifically controlled to be identical across MRI scans in the present study. Nevertheless, the degree of reliability is presented to give a benchmark for how much these parameters can change under normal conditions. A previous study by Martin et al. showed a high degree of inter- and intra-operator reliability for MR-based geometric and hydrodynamic parameters derived from the SAS for a single patient with Chiari malformation and a healthy control subject [54]. 2-week follow-up reliability of these parameters was not considered in that study.

Limitations and future directions

This study provides quantitative measures and reliability assessment for intrathecal CSF dynamics and geometry in eight NHPs. Further studies should quantify potential variance of these parameters in a larger study size across NHP species, age, sex, weight, and in disease states. Geometric characterization did not take into account spinal cord nerve root surface area or volume, which may account for ~231 cm^2 and ~6 ml, respectively within the SAS in humans [52]. It is expected that these structures will alter the SAS surface area results presented in the current study to a large degree. Albeit, the surface area in contact with the spinal cord and dura is likely similar since the junction of spinal cord nerve roots with these structures is relatively small. Also, we do not expect these structures to alter spinal cord and dura surface area to a great degree or total SAS volume.

There are also a few unknowns in relation CSF flow dynamics. First, CSF flow coupling with the cardiovascular cycle is accounted for in the present study. However, CSF flow is also affected by respiration [55], which was not considered in this study using cardiac-gated PC-MRI measurements. Future studies could investigate the relatively contribution of respiration and cardiovascular pulsations to CSF flow dynamics along the spinal axis. Finally, CSF flow was measured at six axial locations and interpolated to generate a smooth distribution along the spine. The ideal study would minimize or eliminate interpolation as much as possible by adding more axial slice locations. Also, CSF dynamics should be quantified within the intracranial space. However, in the present study, MRI time limitation for each NHP did not allow additional slice measurement locations. The focus of the present study was on the intrathecal space, as this region is most nearby intrathecal therapeutic injection location that can be accessed by lumbar puncture or other relatively minimally invasive procedures. Injection of medications within the ventricular space of the brain or cortical subarachnoid space would also be impacted by nearby CSF dynamics within the ventricles and cisterns of the brain.

Conclusions

This study presents a detailed geometric and hydrodynamic characterization of intrathecal CSF for eight cynomolgus monkey (*Macaca fascicularis*) with reliability assessed between baseline and a two-week follow-up time point. Results showed laminar CSF flow along the entire spine with maximum CSF flow rate at the C3-C4 vertebral level and peak systolic CSF flow rate and stroke volume at C3-C4. The methods presented demonstrate a reliable method for CSF quantification in NHPs, which may extend in future studies to *Homo sapiens*.

Supporting information

S1 Table. Source data for the axial distribution of subarachnoid space geometric and hydrodynamic parameters and the CSF flow waveforms collected at different vertebral levels. Data for all eight NHPs measured at baseline and follow-up (T1 and T2).
(XLSX)

Acknowledgments

Publication of this article was funded by the University of Idaho Open Access Publishing Fund

Author Contributions

Conceptualization: Gregory R. Stewart, Bryn A. Martin.

Data curation: Christina P. Gibbs, Joshua J. Pluid, John N. Oshinski, Gregory R. Stewart, Jillynne R. Zeller, Bryn A. Martin.

Formal analysis: Mohammadreza Khani, Lucas R. Sass, Christina P. Gibbs, Joshua J. Pluid, Bryn A. Martin.

Funding acquisition: Bryn A. Martin.

Investigation: Bryn A. Martin.

Methodology: Mohammadreza Khani, Christina P. Gibbs, Joshua J. Pluid, Bryn A. Martin.

Project administration: Bryn A. Martin.

Resources: Bryn A. Martin.

Software: Bryn A. Martin.

Supervision: Bryn A. Martin.

Validation: Bryn A. Martin.

Visualization: Bryn A. Martin.

Writing – original draft: Mohammadreza Khani, Braden J. Lawrence, Lucas R. Sass, Bryn A. Martin.

Writing – review & editing: Mohammadreza Khani, Braden J. Lawrence, Lucas R. Sass, Christina P. Gibbs, Joshua J. Pluid, John N. Oshinski, Gregory R. Stewart, Bryn A. Martin.

References

1. Lawrence BJ, Luciano M, Tew J, Ellenbogen RG, Oshinski JN, et al. (2018) Cardiac-Related Spinal Cord Tissue Motion at the Foramen Magnum is Increased in Patients with Type I Chiari Malformation and Decreases Postdecompression Surgery. World Neurosurg 116: e298–e307. https://doi.org/10.1016/j.wneu.2018.04.191 PMID: 29733988
2. Bert RJ, Hayek SM, Yaksh TL (2017) Modeling Spinal Intrathecal Drug Distribution: The Challenge of Defining and Predicting Cerebrospinal Fluid Dynamics. Anesth Analg 124: 1403–1406. https://doi.org/10.1213/ANE.0000000000002071 PMID: 28426585
3. Brinker T, Stopa E, Morrison J, Klinge PJF, CNS Bot (2014) A new look at cerebrospinal fluid circulation. 11: 10.
4. Enzmann DR, Pelc NJ (1991) Normal flow patterns of intracranial and spinal cerebrospinal fluid defined with phase-contrast cine MR imaging. Radiology 178: 467–474. https://doi.org/10.1148/radiology.178.2.1987610 PMID: 1987610
5. Schroth G, Klose U (1992) Cerebrospinal-Fluid Flow .2. Physiology of Respiration-Related Pulsations. Neuroradiology 35: 10–15. PMID: 1289732
6. Martin BA, Labuda R, Royston TJ, Oshinski JN, Iskandar B, et al. (2010) Spinal subarachnoid space pressure measurements in an in vitro spinal stenosis model: implications on syringomyelia theories. J Biomech Eng 132: 111007. https://doi.org/10.1115/1.4000089 PMID: 21034148
7. Wostyn P, Audenaert K, De Deyn PP (2009) More advanced Alzheimer's disease may be associated with a decrease in cerebrospinal fluid pressure. Cerebrospinal Fluid Res 6: 14. https://doi.org/10.1186/1743-8454-6-14 PMID: 19917128
8. Bunck AC, Kroeger JR, Juettner A, Brentrup A, Fiedler B, et al. (2012) Magnetic resonance 4D flow analysis of cerebrospinal fluid dynamics in Chiari I malformation with and without syringomyelia. Eur Radiol 22: 1860–1870. https://doi.org/10.1007/s00330-012-2457-7 PMID: 22569996
9. Bradley WG Jr., Kortman KE, Burgoyne B (1986) Flowing cerebrospinal fluid in normal and hydrocephalic states: appearance on MR images. Radiology 159: 611–616. https://doi.org/10.1148/radiology.159.3.3704142 PMID: 3704142
10. Pizzichelli G, Kehlet B, Evju O, Martin BA, Rognes ME, et al. (2017) Numerical study of intrathecal drug delivery to a permeable spinal cord: effect of catheter position and angle. Comput Methods Biomech Biomed Engin: 1–10.

11. Khani M, Xing T, Gibbs C, Oshinski JN, Stewart GR, et al. (2017) Nonuniform Moving Boundary Method for Computational Fluid Dynamics Simulation of Intrathecal Cerebrospinal Flow Distribution in a Cynomolgus Monkey. J Biomech Eng 139.
12. Khani M, Sass L, Xing T, Sharp MK, Balédent O, et al. (2018) Anthropomorphic Model of Intrathecal Cerebrospinal Fluid Dynamics Within the Spinal Subarachnoid Space: Spinal Cord Nerve Roots Increase Steady-Streaming. Journal of Biomechanical Engineering.
13. Tangen K, Narasimhan NS, Sierzega K, Preden T, Alaraj A, et al. (2016) Clearance of Subarachnoid Hemorrhage from the Cerebrospinal Fluid in Computational and In Vitro Models. Ann Biomed Eng.
14. Tangen KM, Leval R, Mehta AI, Linninger AA (2017) Computational and in vitro experimental investigation of intrathecal drug distribution: parametric study of the effect of injection volume, cerebrospinal fluid pulsatility, and drug uptake. Anesthesia & Analgesia 124: 1686–1696.
15. Greitz D, Hannerz J (1996) A proposed model of cerebrospinal fluid circulation: Observations with radionuclide cisternography. American Journal of Neuroradiology 17: 431–438. PMID: 8881235
16. Papisov MI, Belov VV, Gannon KS (2013) Physiology of the Intrathecal Bolus: The Leptomeningeal Route for Macromolecule and Particle Delivery to CNS. Mol Pharm 10: 1522–1532. https://doi.org/10.1021/mp300474m PMID: 23316936
17. Puy V, Zmudka-Attier J, Capel C, Bouzerar R, Serot JM, et al. (2016) Interactions between Flow Oscillations and Biochemical Parameters in the Cerebrospinal Fluid. Frontiers in Aging Neuroscience 8.
18. O'Donnell J, Ding F, Nedergaard M (2015) Distinct functional states of astrocytes during sleep and wakefulness: Is norepinephrine the master regulator? Curr Sleep Med Rep 1: 1–8. https://doi.org/10.1007/s40675-014-0004-6 PMID: 26618103
19. Xie L, Kang H, Xu Q, Chen MJ, Liao Y, et al. (2013) Sleep drives metabolite clearance from the adult brain. Science 342: 373–377. https://doi.org/10.1126/science.1241224 PMID: 24136970
20. Patel T, Zhou J, Piepmeier JM, Saltzman WM (2012) Polymeric nanoparticles for drug delivery to the central nervous system. Adv Drug Deliv Rev 64: 701–705. https://doi.org/10.1016/j.addr.2011.12.006 PMID: 22210134
21. Lu CT, Zhao YZ, Wong HL, Cai J, Peng L, et al. (2014) Current approaches to enhance CNS delivery of drugs across the brain barriers. Int J Nanomedicine 9: 2241–2257. https://doi.org/10.2147/IJN.S61288 PMID: 24872687
22. Watanabe Y, Kazuki Y, Kazuki K, Ebiki M, Nakanishi M, et al. (2015) Use of a Human Artificial Chromosome for Delivering Trophic Factors in a Rodent Model of Amyotrophic Lateral Sclerosis. Mol Ther Nucleic Acids 4: e253. https://doi.org/10.1038/mtna.2015.28 PMID: 26440597
23. Deepa P, Shahani N, Alladi PA, Vijayalakshmi K, Sathyaprabha TN, et al. (2011) Down regulation of trophic factors in neonatal rat spinal cord after administration of cerebrospinal fluid from sporadic amyotrophic lateral sclerosis patients. J Neural Transm (Vienna) 118: 531–538.
24. Chen BK, Staff NP, Knight AM, Nesbitt JJ, Butler GW, et al. (2015) A safety study on intrathecal delivery of autologous mesenchymal stromal cells in rabbits directly supporting Phase I human trials. Transfusion 55: 1013–1020. https://doi.org/10.1111/trf.12938 PMID: 25413276
25. Katz N, Goode T, Hinderer C, Hordeaux J, Wilson JM (2018) Standardized method for intra-cisterna magna delivery under fluoroscopic guidance in nonhuman primates. Hum Gene Ther Methods.
26. Miller TM, Pestronk A, David W, Rothstein J, Simpson E, et al. (2013) An antisense oligonucleotide against SOD1 delivered intrathecally for patients with SOD1 familial amyotrophic lateral sclerosis: a phase 1, randomised, first-in-man study. Lancet Neurol 12: 435–442. https://doi.org/10.1016/S1474-4422(13)70061-9 PMID: 23541756
27. Ordia JI, Fischer E, Adamski E, Spatz EL (1996) Chronic intrathecal delivery of baclofen by a programmable pump for the treatment of severe spasticity. J Neurosurg 85: 452–457. https://doi.org/10.3171/jns.1996.85.3.0452 PMID: 8751632
28. Claborn MK, Stevens DL, Walker CK, Gildon BL (2018) Nusinersen: A Treatment for Spinal Muscular Atrophy. Ann Pharmacother: 1060028018789956. https://doi.org/10.1177/1060028018789956 PMID: 30008228
29. Martin BA, Kalata W, Shaffer N, Fischer P, Luciano M, et al. (2013) Hydrodynamic and longitudinal impedance analysis of cerebrospinal fluid dynamics at the craniovertebral junction in type I Chiari malformation. PLoS One 8: e75335. https://doi.org/10.1371/journal.pone.0075335 PMID: 24130704
30. Yushkevich PA, Piven J, Hazlett HC, Smith RG, Ho S, et al. (2006) User-guided 3D active contour segmentation of anatomical structures: significantly improved efficiency and reliability. Neuroimage 31: 1116–1128. https://doi.org/10.1016/j.neuroimage.2006.01.015 PMID: 16545965
31. Martin BA, Yiallourou TI, Pahlavian SH, Thyagaraj S, Bunck AC, et al. (2016) Inter-operator Reliability of Magnetic Resonance Image-Based Computational Fluid Dynamics Prediction of Cerebrospinal Fluid

Motion in the Cervical Spine. Ann Biomed Eng 44: 1524–1537. https://doi.org/10.1007/s10439-015-1449-6 PMID: 26446009

32. Kalata W, Martin BA, Oshinski JN, Jerosch-Herold M, Royston TJ, et al. (2009) MR Measurement of Cerebrospinal Fluid Velocity Wave Speed in the Spinal Canal. IEEE Trans Biomed Eng.
33. Yiallourou TI, Kroger JR, Stergiopulos N, Maintz D, Martin BA, et al. (2012) Comparison of 4D phase-contrast MRI flow measurements to computational fluid dynamics simulations of cerebrospinal fluid motion in the cervical spine. PLoS One 7: e52284. https://doi.org/10.1371/journal.pone.0052284 PMID: 23284970
34. Jain K, Ringstad G, Eide PK, Mardal KA (2017) Direct numerical simulation of transitional hydrodynamics of the cerebrospinal fluid in Chiari I malformation: The role of cranio-vertebral junction. International Journal for Numerical Methods in Biomedical Engineering 33.
35. Loth F, Yardimci MA, Alperin N (2001) Hydrodynamic modeling of cerebrospinal fluid motion within the spinal cavity. J Biomech Eng 123: 71–79. PMID: 11277305
36. Khani M, Sass LR, Xing T, Keith Sharp M, Balédent O, et al. (2018) Anthropomorphic Model of Intrathecal Cerebrospinal Fluid Dynamics Within the Spinal Subarachnoid Space: Spinal Cord Nerve Roots Increase Steady-Streaming. Journal of Biomechanical Engineering 140: 081012-081012-081015.
37. Williams B (1981) Simultaneous cerebral and spinal fluid pressure recordings. I. Technique, physiology, and normal results. Acta Neurochir (Wien) 58: 167–185.
38. Sweetman B, Linninger AA (2011) Cerebrospinal fluid flow dynamics in the central nervous system. Ann Biomed Eng 39: 484–496. https://doi.org/10.1007/s10439-010-0141-0 PMID: 20737291
39. Martin BA, Reymond P, Novy J, Baledent O, Stergiopulos N (2012) A coupled hydrodynamic model of the cardiovascular and cerebrospinal fluid system. Am J Physiol Heart Circ Physiol 302: H1492–1509. https://doi.org/10.1152/ajpheart.00658.2011 PMID: 22268106
40. Martin BA, Labuda R, Royston TJ, Oshinski JN, Iskandar B, et al. (2010) Spinal Subarachnoid Space Pressure Measurements in an In Vitro Spinal Stenosis Model: Implications on Syringomyelia Theories. Journal of Biomechanical Engineering-Transactions of the Asme 132.
41. Bertram CD (2010) Evaluation by fluid/structure-interaction spinal-cord simulation of the effects of subarachnoid-space stenosis on an adjacent syrinx. J Biomech Eng 132: 061009. https://doi.org/10.1115/1.4001165 PMID: 20887034
42. Elliott NSJ, Bertram CD, Martin BA, Brodbelt AR (2013) Syringomyelia: A review of the biomechanics. Journal of Fluids and Structures 40: 1–24.
43. Cirovic S, Kim M (2012) A one-dimensional model of the spinal cerebrospinal-fluid compartment. J Biomech Eng 134: 021005. https://doi.org/10.1115/1.4005853 PMID: 22482672
44. Cirovic S, Lloyd R, Jovanovik J, Volk HA, Rusbridge C (2018) Computer simulation of syringomyelia in dogs. BMC Vet Res 14: 82. https://doi.org/10.1186/s12917-018-1410-7 PMID: 29523203
45. Vardoulis O, Coppens E, Martin BA, Reymond P, Tozzi P, et al. (2011) Impact of Aortic Grafts on Arterial Pressure: A Computational Fluid Dynamics Study. European Journal of Vascular and Endovascular Surgery 42: 704–710. https://doi.org/10.1016/j.ejvs.2011.08.006 PMID: 21889370
46. Reymond P, Perren F, Lazeyras F, Stergiopulos N (2012) Patient-specific mean pressure drop in the systemic arterial tree, a comparison between 1-D and 3-D models. J Biomech 45: 2499–2505. https://doi.org/10.1016/j.jbiomech.2012.07.020 PMID: 22884968
47. Bilston LE, Stoodley MA, Fletcher DF (2010) The influence of the relative timing of arterial and subarachnoid space pulse waves on spinal perivascular cerebrospinal fluid flow as a possible factor in syrinx development. J Neurosurg 112: 808–813. https://doi.org/10.3171/2009.5.JNS08945 PMID: 19522574
48. Hemley SJ, Bilston LE, Cheng S, Chan JN, Stoodley MA (2013) Aquaporin-4 expression in post-traumatic syringomyelia. J Neurotrauma 30: 1457–1467. https://doi.org/10.1089/neu.2012.2614 PMID: 23441695
49. Yeo J, Cheng S, Hemley S, Lee BB, Stoodley M, et al. (2017) Characteristics of CSF Velocity-Time Profile in Posttraumatic Syringomyelia. AJNR Am J Neuroradiol.
50. Gray SJ, Nagabhushan Kalburgi S, McCown TJ, Jude Samulski R (2013) Global CNS gene delivery and evasion of anti-AAV-neutralizing antibodies by intrathecal AAV administration in non-human primates. Gene Ther 20: 450–459. https://doi.org/10.1038/gt.2012.101 PMID: 23303281
51. Hall JE, Guyton AC (2011) Guyton and Hall textbook of medical physiology. Philadelphia, Pa.: Saunders/Elsevier. xix, 1091 p. p.
52. Sass LR, Khani M, Natividad GC, Tubbs RS, Baledent O, et al. (2017) A 3D subject-specific model of the spinal subarachnoid space with anatomically realistic ventral and dorsal spinal cord nerve rootlets. Fluids and Barriers of the CNS 14: 36. https://doi.org/10.1186/s12987-017-0085-y PMID: 29258534

53. Levi Chazen J, Dyke JP, Holt RW, Horky L, Pauplis RA, et al. (2017) Automated segmentation of MR imaging to determine normative central nervous system cerebrospinal fluid volumes in healthy volunteers. Clin Imaging 43: 132–135. https://doi.org/10.1016/j.clinimag.2017.02.007 PMID: 28314198

54. Martin BA, Yiallourou TI, Pahlavian SH, Thyagaraj S, Bunck AC, et al. (2016) Inter-operator Reliability of Magnetic Resonance Image-Based Computational Fluid Dynamics Prediction of Cerebrospinal Fluid Motion in the Cervical Spine. Annals of Biomedical Engineering Accepted.

55. Yildiz S, Thyagaraj S, Jin N, Zhong X, Heidari Pahlavian S, et al. (2017) Quantifying the influence of respiration and cardiac pulsations on cerebrospinal fluid dynamics using real-time phase-contrast MRI. J Magn Reson Imaging 46: 431–439. https://doi.org/10.1002/jmri.25591 PMID: 28152239